CrossMark

Hot Deformation and Corrosion Resistance of High-Strength Low-Alloy Steel

Wilasinee Kingkam[1] · Cheng-Zhi Zhao[1,2] · Hong Li[1] · He-Xin Zhang[1,2] · Zhi-Ming Li[3]

Abstract

The hot deformation characteristics and the corrosion behavior of a high-strength low-alloy (HSLA) steel were investigated at deformation temperatures ranging from 800 to 1100 °C and strain rates ranging from 0.1 to 10 s^{-1} using an MMS-200 thermal simulation testing machine. Based on the flow curves from the experiment, the effects of temperature and strain rate on the dynamic recrystallization behavior were analyzed. The flow stress decreased with increasing deformation temperature and decreasing strain rate. With the assistance of the process parameters, constitutive equations were used to obtain the activation energy and hot working equation. The hot deformation activation energy of HSLA steel in this work was 351.87 kJ/mol. The work hardening rate was used to determine the critical stress (strain) or the peak stress (strain). The dependence of these characteristic values on the Zener–Hollomon parameter was found. A dynamic recrystallization kinetics model of the tested HSLA steel was constructed, and the validity of the model was confirmed by the experimental results. Observation of the microstructures indicated that the grain size increased with increasing deformation temperature, which led to a lowered corrosion resistance of the specimens.

Keywords Dynamic recrystallization · Potentiodynamic polarization · Hot deformation · Flow stress · High-strength low-alloy steel

1 Introduction

High-strength low-alloy (HSLA) steels are important structural materials that contain small amounts of alloying elements such as niobium, titanium, vanadium, and aluminum, which enhance the strength of the steels through the formation of stable carbides, nitrides, and carbonitrides and provide greater resistance to atmospheric corrosion than conventional carbon steels. These steels are widely used in oil pipelines and transport industries and exhibit a good combination of weldability and mechanical performance [1–4]. However, considering the material requirements for use in transport pipelines, improvement in the corrosion resistance of HSLA steel in seawater is necessary. Chloride ions in seawater have been reported to cause pitting corrosion of carbon steel, which can lead to a significant reduction in the lifetime of the steel. Chloride ions can penetrate through the corrosion product layer, especially via defects, and can reach the base metal surface [5–7]. The presence of chloride ions frequently causes the passive film formed on the metal surface to break down [8, 9] and exacerbates stress corrosion cracking (SCC) failures for most martensitic stainless steels and HSLA steels [10].

The corrosion behaviors of HSLA steel have been paid much attention [11–14], but few investigations have focused on the effects of variations in microstructure on the corrosion behavior. The inhibitor efficiency of the corrosion layers is closely related to the microstructures of alloy steels. The microstructure evolution during deformation at an elevated temperature affects the strain and strain rate heavily and properties of HSLA steel [15]. The dynamic

✉ He-Xin Zhang
  zhanghx@hrbeu.edu.cn

1   College of Materials Science and Chemical Engineering, Harbin Engineering University, Harbin 150001, China

2   Key Laboratory of Superlight Materials and Surface Technology, Ministry of Education, Harbin Engineering University, Harbin 150001, China

3   College of Power and Energy Engineering, Harbin Engineering University, Harbin 150001, China

recrystallization (DRX) is an important mechanism for microstructure control during hot deformation [16, 17]. Predicting the critical conditions for the initiation of DRX is also significant in modeling industrial processes. Several researchers have predicted DRX phenomena during deformation. For example, Ryan and Mcqueen [18] suggested that the initiation of DRX can be identified from changes in the slope between the work hardening and the flow stress. Saadatkia et al. [19] proposed work hardening rate plots that are used to determine the critical conditions for the onset of DRX. However, there have been few research studies on the hot deformation behavior and dynamic recrystallization of HSLA steel that is conducive to optimizing the process parameters and improving the corrosion resistance of steel through hot deformation.

In this study, the components of the material constants for the Arrhenius equation are investigated using flow stress data and quantitative equations to predict the kinetic of DRX behavior based on the hot deformation parameters, and the effects of DRX and deformation temperature during hot deformation on the corrosion resistance of HSLA steel are discussed.

2 Experimental

The chemical composition (wt%) of the HSLA steel used in this investigation was as follows: 0.01 C, 0.213 Cr, 0.14 Si, 1.38 Mn, 0.514 Ni, 0.39 Cu, 0.135 Mo, 0.027 Nb, 0.009 V and balance Fe. The HSLA cast steel was cut into cylindrical specimens with size $\Phi 8 \times 15$ mm. The longitudinal direction of the cylindrical specimens was parallel to the axial compression direction. Hot compression of the cylinders was performed from 800 to 1100 °C with strain rates of 0.1, 1 and 10 s^{-1} on an MMS-200 thermal simulation testing machine. The specimens were heated from room temperature to 1250 °C at a heating rate of 20 °C/s and held for 5 min. Compression tests of all the specimens were carried out to a total true strain of $\sim$ 0.65, and then, all the specimens were immediately quenched in water. Schematic illustrations of the uniaxial compression tests and the specimen geometry are shown in Fig. 1.

The electrochemical tests of the HSLA steel were conducted using the Zennium electrochemistry workstation (ZAHNER-Elektrik. GmbH & Co. KG, Germany) with a standard three-electrode cell with the specimen as the working electrode, a platinum foil as the counter electrode and a silver/silver chloride electrode (Ag/AgCl) as the reference electrode. The polarization curves were measured in 1 mol/L NaCl solution at room temperature, between −1.6 and 0.2 V, with a scan rate of 1 mV/s. All specimens acting as working electrodes were embedded in epoxy resin.

3 Results and Discussion

3.1 Flow Curves Behavior

The true stress–strain curves for the HSLA steel that were obtained at various strain rates in the deformation temperature range of 800–1100 °C are shown in Fig. 2. All of the flow curves are sensitively dependent on temperature and strain rate; the flow stress decreases with increasing deformation temperature and decreasing strain rate. The flow stress curves are composed of three stages: stage I (work hardening stage), stage II (softening stage) and stage III (steady-state stage) [20, 21]. In the first stage, the flow stress exhibits a rapid increase to a critical value and the number of dislocations continually increases and then rapidly accumulates, resulting in work hardening. Meanwhile, the dynamic recovery (DRV) effects during this stage are too weak to balance the effects of the work hardening. In the second stage, the flow stress increases at a decreasing rate until a peak value or an inflection of the work hardening rate is reached, which shows that the thermal softening due to dynamic recrystallization (DRX) and dynamic recovery (DRV) becomes increasingly dominant, eventually exceeding the effects of the work hardening. In the softening stage, the accumulated dislocation density exceeds a critical strain, and DRX takes place. The nucleation and growth of dynamic recrystallized grains can cause dislocation annihilation, which decreases the flow stress. In the third stage, the flow stress reaches steady state due to a dynamic balance between the work hardening and dynamic softening [22, 48].

The effects of strain rate and deformation temperature on flow stress can be explained in terms of dislocation mechanisms and DRX, which are mainly affected by the deformation mechanisms. At the strain rate of 0.1 s^{-1}, the flow curves show a single peak followed by decreasing stress and finally reach a plateau, which implies that DRX occurs. At the strain rates of 1 and 10 s^{-1}, the flow curves show dynamic recovery (DRV) character without peak stress. The results indicated that there was not sufficient time for the nucleation and growth of new DRX grains or for dislocation annihilation at higher strain rates and lower temperatures [23–25]. Thus, it is seen that the HSLA steel has negative temperature sensitivity and positive strain rate sensitivity [26].

3.2 Constitutive Modeling

Constitutive equations are widely used to model metals and alloys during hot deformation at elevated temperatures and strain rates. The constitutive model is related to temperature, flow stress and strain rate and can be expressed by the
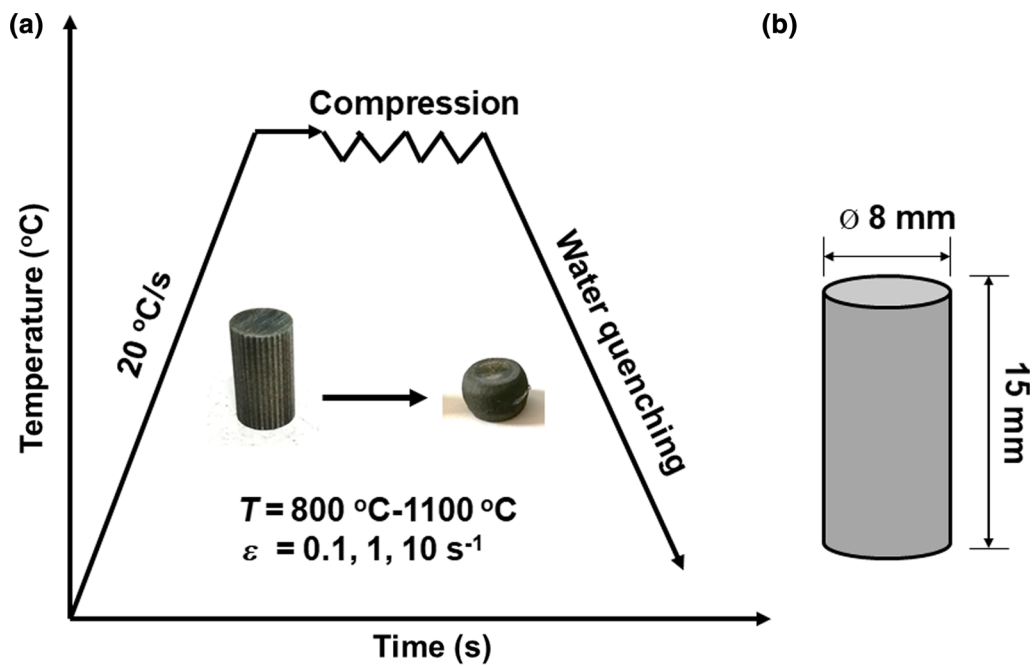
Fig. 1 Schematic illustrations of **a** uniaxial compression tests, **b** specimen geometry of HSLA steel
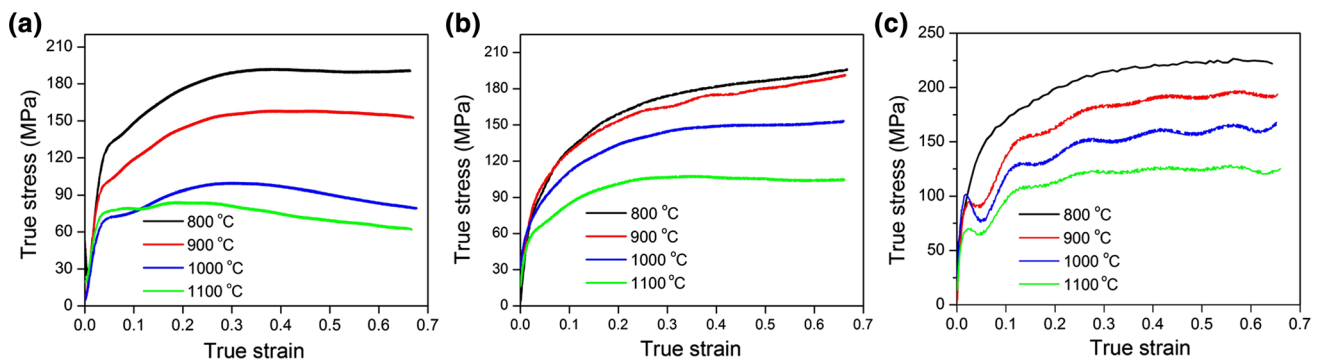

Fig. 2 True stress–strain curves for HSLA steel at strain rates of **a** 0.1 s^{-1}, **b** 1 s^{-1}, **c** 10 s^{-1}

hyperbolic sine function form of the Arrhenius type equation [27, 28] as follows:

$$\dot{\varepsilon} = A f(\sigma) \exp\left(-\frac{Q}{R_g T}\right), \tag{1}$$

where $\dot{\varepsilon}$ is the strain rate (s^{-1}), σ is the flow stress (MPa), Q is the activation energy of hot deformation (kJ/mol^{-1}), T is the absolute temperature (K), A is a material constant, R_g is the universal gas constant (8.31 J/(mol K)) and $f(\sigma)$ is the stress function, which can be expressed as follows:

$$f(\sigma) = \begin{cases} \sigma^{n_1} & (\alpha\sigma < 0.8) \\ \exp(\beta\sigma) & (\alpha\sigma > 1.2), \\ [\sinh(\alpha\sigma)]^n & (\text{all } \sigma) \end{cases} \tag{2}$$

where β, n_1, α and n are material constants. The correlation between strain rate and temperature for hot deformation

behavior can be expressed by the Zener–Hollomon parameter as follows:

$$Z = \dot{\varepsilon} \exp\left(\frac{Q}{RT}\right), \tag{3}$$

where Z is the Zener–Hollomon parameter and $\alpha = \beta/n_1$ is a stress multiplier. At low ($\alpha\sigma < 0.8$), high ($\alpha\sigma > 1.2$), and all stress levels, substituting (the power law and exponential law) Eq. (3) into Eq. (1) with the suitable function and taking the natural logarithm of both sides leads to Eqs. (4)–(6) as follows:

$$\ln\dot{\varepsilon} = n_1 \ln\sigma + \ln A - Q/(RT), \tag{4}$$

$$\ln\dot{\varepsilon} = \beta\sigma + \ln A - Q/(RT), \tag{5}$$

$$\ln\dot{\varepsilon} = \ln A + n\ln[\sinh(\alpha\sigma)] - Q/(RT). \tag{6}$$

According to Eqs. (4) and (5), the values of n_1 and β can be obtained from the slopes of $\ln\dot{\varepsilon} - \sigma$ and $\ln\dot{\varepsilon} - \ln\sigma$, as shown in Fig. 3a, b, by using linear regression and averaging with the resulting constant values as follows: $n_1 = 14.89$, $\beta = 0.094$ and $\alpha = 0.0063$. For all stresses (including low and high stress levels) in Eq. (6), the slopes of the linear regression fits for the $\ln\dot{\varepsilon} - \ln[\sinh(\alpha\sigma)]$ plots can be obtained, as shown in Fig. 3c. The average value of the materials constant (n) is 11.05.

For a given strain rate and temperature condition, together with the linear relationship between $\ln[\sinh(\alpha\sigma)]$ and $1000/T$ and Eq. (6), the activation energy (Q) can be obtained from the following equation:

$$Q = Rn\left[\frac{\partial\ln[\sinh(\alpha\sigma)]}{\partial(1/T)}\right]_{\dot{\varepsilon}}. \tag{7}$$

The values for Q can be calculated using the slopes of the linear regression fits for the $\ln[\sinh(\alpha\sigma)]$ and $1000/T$ plots in Fig. 3d. The average value for Q is 351.877 kJ/mol. It is well known that Q values for hot deformation are a function of chemical composition. Compared with the previous research, the Q value from the current work is comparable with that of Fe-0.5C-2Cu steel (low-carbon steel) and

microalloy steels with a range of Q values from 353 kJ/mol to 375 kJ/mol [29, 30]. The activation energy is sensitive to any change in the chemical composition of alloyed steels, and the value of Q increases with increasing carbon content.

From Eq. (7), the intercepts of the linear regression fits of the $\ln\dot{\varepsilon} - \ln[\sinh(\alpha\sigma)]$ plots can be used to calculate the values for $\ln A$. With the assistance of the calculated parameters mentioned above, the value of material constant A is determined to be 2.81×10^{12}. Then, substituting A, n, α, Q and R into Eq. (1), the hot working equation for describing the relationship between $\dot{\varepsilon}$, T and σ can be expressed as follows:

$$\dot{\varepsilon} = 2.81 \times 10^{12}[\sinh(0.0063\sigma)]^{11.05}\exp\left(-\frac{351877}{RT}\right), \tag{8}$$

3.3 Work Hardening Rates of Flow Stress Curves

Work hardening characteristics during hot deformation processing indicate complex behavior from the effects of deformation parameters such as the stress, strain rate
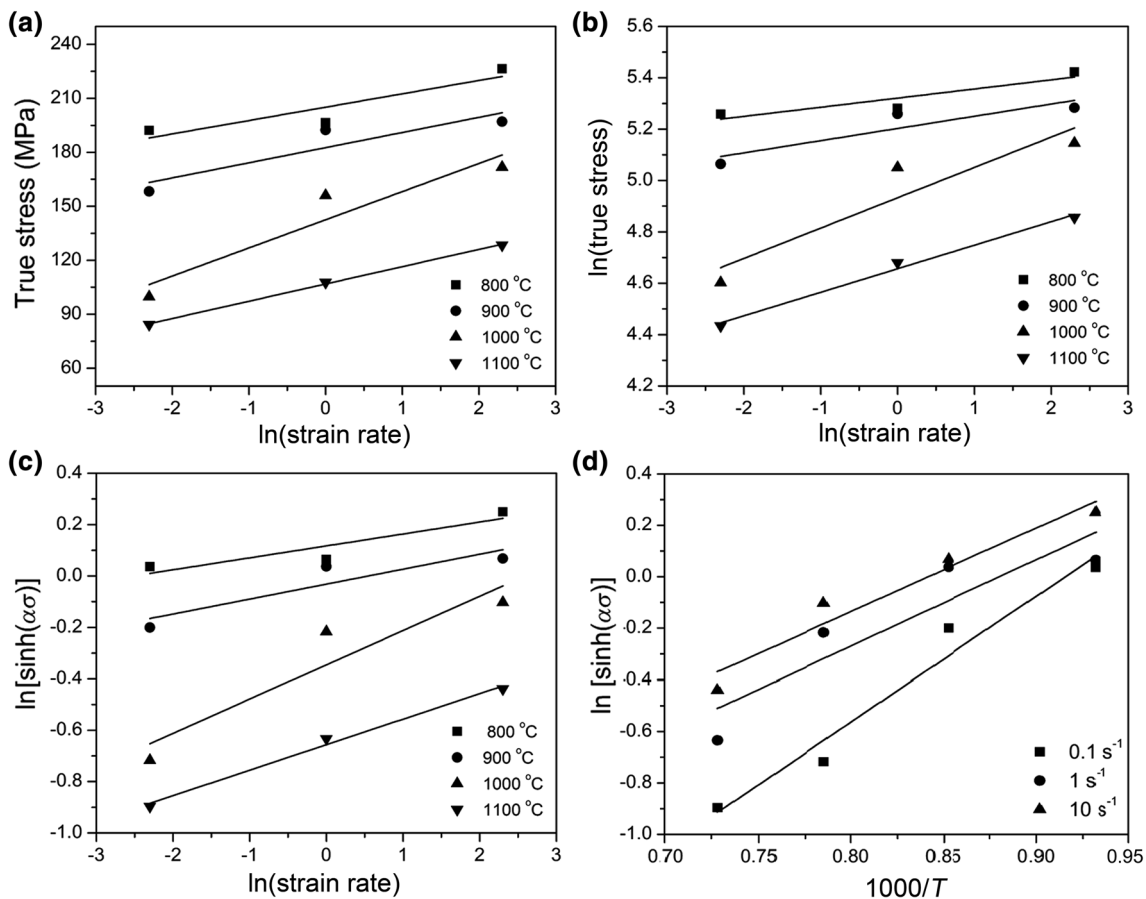

Fig. 3 Relationships of a $\ln\dot{\varepsilon} - \sigma$, b $\ln\dot{\varepsilon} - \ln\sigma$, c $\ln\dot{\varepsilon} - \ln[\sinh(\alpha\sigma)]$, d $\ln[\sinh(\alpha\sigma)]-1000/T$

sensitivity, and temperature. The work hardening behavior is usually analyzed by investigating the variation of the work hardening rate ($\theta = \mathrm{d}\sigma/\mathrm{d}\varepsilon$) with true stress and true strain measurements [31]. Moreover, the work hardening behavior is used to identify different characteristic points in the flow curves that correspond to mechanisms of microstructure evolution. Several characteristic parameters, such as the critical stress (σ_c) and critical strain (ε_c), for the initiation of dynamic recrystallization are determined from changes in the shape of the work hardening curve. Likewise, the quantified parameters related to DRX behavior are the key factors considered in the construction of the DRX kinetics model.

Figure 4 shows the $\theta-\sigma$ curves for HSLA steel deformed at strain rates ranging from 0.1 to 10 s^{-1}. From this figure, the work hardening curves linearly decrease with increasing stress at low stresses due to dynamic recovery. When flow stress increases, the curves gradually decrease in slope and then drop toward $\theta = 0$ at peak stress [32]; then, the work hardening rate curves intersect with the true stress (σ) axis again, and flow stress becomes steady-state stress. The relationships between work hardening and true strain at a strain rate of 0.1 s^{-1} are shown in Fig. 5. In all cases, the work hardening decreases with increasing strain in the initial stage and then saturates with increasing strain. The critical stress (σ_c), critical strain (ε_c), peak stress (σ_p), peak strain (ε_p) and onset of steady-state stress (σ_{ss}) can be determined using the curves from the relationships between $\theta-\sigma$ and $\theta-\varepsilon$. The values measured for critical stress and critical strain are listed in Table 1. When the deformation temperature is constant, the parameters for work hardening increase with increasing strain rate. When strain rate is constant, these parameters decrease with increasing deformation temperature. Figure 7 shows the relationship between σ_c (ε_c) and σ_p (ε_p). The correlations between the critical parameters and the peak parameters can be determined by linear regression analysis, and the following equations are obtained:

$$\sigma_c = 0.78\sigma_p, \tag{9}$$

$$\varepsilon_c = 0.42\varepsilon_p. \tag{10}$$

Previous researches [33–35] have reported that the ratio of critical strain and peak strain is generally between 0.6 and 0.8. However, lower values in the range of 0.37–0.5 have also been reported for some steels, such as vanadium microalloyed steel, X7 pipeline steels, and low-carbon vanadium-nitride microalloyed steel [36–38]. Therefore, the result in this paper is in reasonable agreement with the previous research mentioned above, which indicates that the chemical composition of alloy steel has a minimal effect on these parameters. According to Fig. 6, the normalized critical stress and strain are expressed by $\sigma_c/\sigma_p = 0.83$ and $\varepsilon_c/\varepsilon_p = 0.307$, respectively.

The relationships between critical stress σ_c (strain ε_c) and Z and peak stress σ_p (strain ε_p) and Z are shown in Fig. 7. The $\ln\sigma_c$ ($\ln\varepsilon_c$) and $\ln\sigma_p$ ($\ln\varepsilon_p$) versus $\ln Z$ relationships are linear. By linear regression analysis, the following equations are obtained:

$$\sigma_p = 9.68Z^{0.07}, \tag{11}$$

$$\sigma_c = 9.025Z^{0.067}, \tag{12}$$

$$\varepsilon_p = 0.033Z^{0.061}, \tag{13}$$

$$\varepsilon_c = 0.003Z^{0.095}. \tag{14}$$

An increase in the value of Z leads to higher values for $\ln\sigma_c$ ($\ln\varepsilon_c$) or $\ln\sigma_p$ ($\ln\varepsilon_p$). Therefore, the occurrence of DRX is probably difficult [38]. On the other hand, DRX can occur at smaller strains with decreasing values of the Z parameter.

3.4 DRX Kinetic Model

The DRX volume fraction (X_d) is often calculated from the peak strain obtained from the flow curve, which indicates
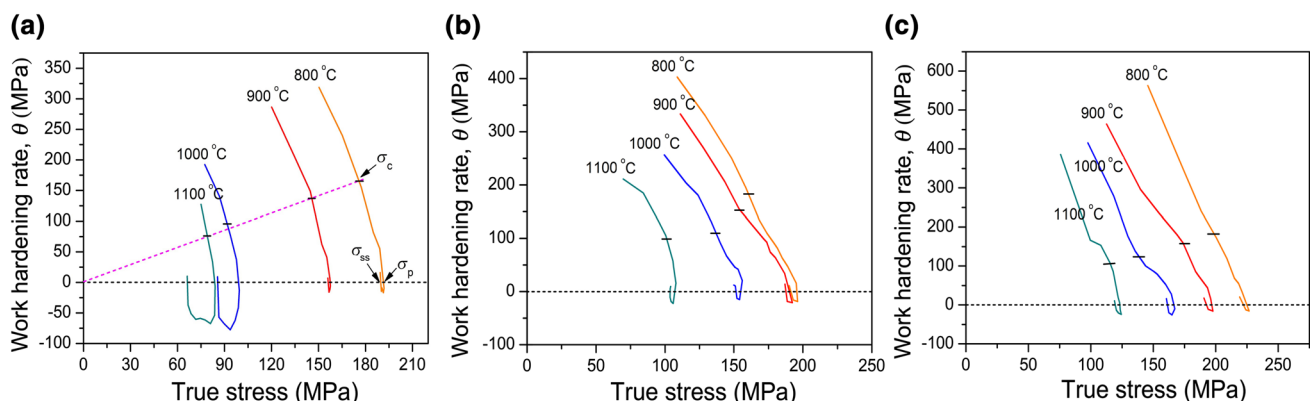

Fig. 4 Relationships between $\theta-\sigma$ under strain rate of **a** $\dot{\varepsilon} = 0.1$ s^{-1}, **b** $\dot{\varepsilon} = 1$ s^{-1}, **c** $\dot{\varepsilon} = 10$ s^{-1}
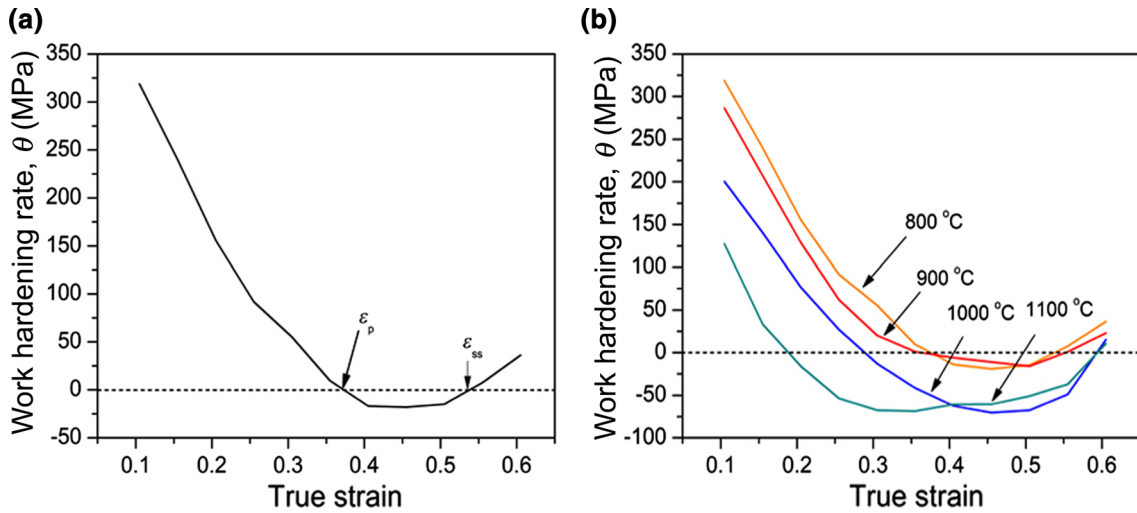
Fig. 5 Relationships between θ–ε at **a** 800 °C, 0.1 s^{-1}, **b** various temperatures with strain rate of 0.1 s^{-1}

Table 1 Values of critical strain and critical stress under various deformation temperatures and strain rates

Temperature (°C)	Strain rate (s^{-1})					
	0.1		1		10	
	σ_c	ε_c	σ_c	ε_c	σ_c	ε_c
800	160.95	0.151	185.5	0.172	184.58	0.199
900	131.14	0.104	159.72	0.15	153.44	0.17
1000	97.37	0.07	100.44	0.121	139.2	0.152
1100	74.35	0.04	96.09	0.102	100.66	0.11

the onset of kinetic DRX, which continues to the steady-state strain point and is expressed as follows:

$$X_d = \frac{\sigma_p - \sigma}{\sigma_p - \sigma_{ss}}. \tag{15}$$

During hot deformation processing, dislocations continually increase and accumulate to such an extent that at a critical strain, DRX nuclei form and grow near grain boundaries, twin boundaries, and deformation bands. It is well known that the conflicting forces of the multiplication of dislocations due to continual hot deformation and the annihilation of dislocations due to DRX coexist. When work hardening corresponding to the former and DRX softening corresponding to the latter are in dynamic balance, flow stress stays constant with increasing strain, while the deformation enters a steady-state stage in which the DRX grains are completed. In general, the kinetics of DRX can be described in terms of S-curves of the recrystallized volume expressed as a function of time [49]. Therefore, the kinetics of DRX evolution can be predicted by using an Avrami model as follows [39, 40]:
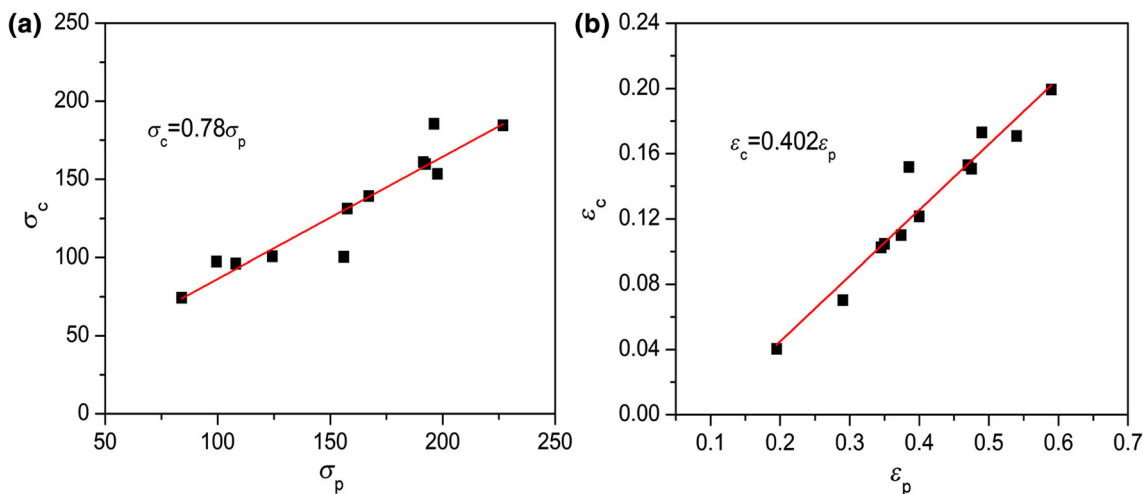

Fig. 6 Relationships of **a** σ_c versus σ_p, **b** ε_c versus ε_p
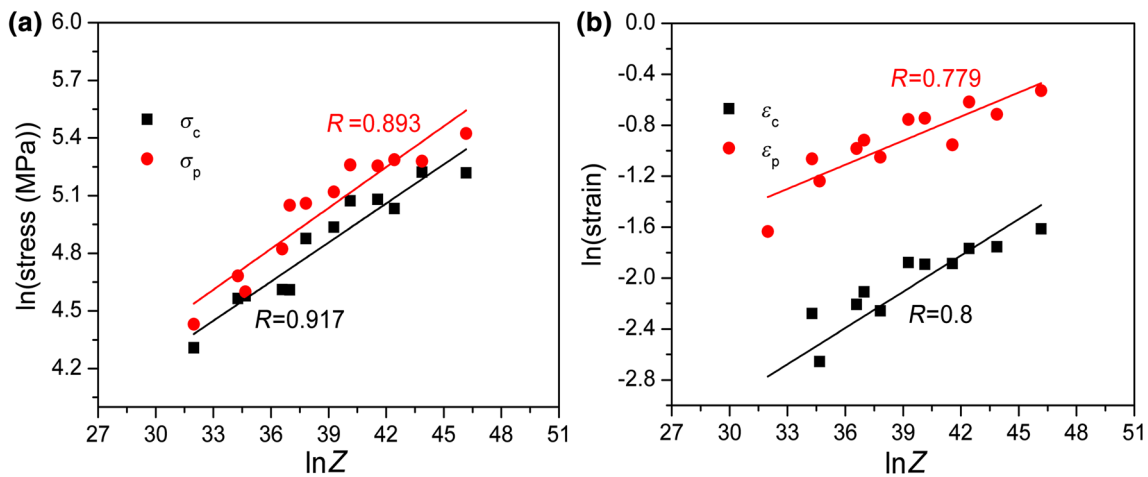
Fig. 7 Relationships between characteristic parameters and Z parameters: **a** $\ln\sigma_p$ and $\ln\sigma_c$ versus $\ln Z$; **b** $\ln\varepsilon_p$ and $\ln\varepsilon_c$ versus $\ln Z$ (R: R-squared value)

$$X_d = 1 - \exp\left[(-k) \cdot \left(\frac{\varepsilon - \varepsilon_p}{\varepsilon_p}\right)^m\right], \quad (16)$$

where k and m are material constants, which can be determined by taking the natural logarithm on both sides of Eq. (16) and rearranging as follows:

$$\ln\left[\ln\left(\frac{1}{1 - X_d}\right)\right] = \ln k + m \ln\left(\frac{\varepsilon - \varepsilon_c}{\varepsilon_p}\right). \quad (17)$$

According to Eq. (17), the linear relationship between the plots of $\ln[\ln[1/(1-X_d)]]$ and $\ln[(\varepsilon-\varepsilon_c)/\varepsilon_p]$, as shown in Fig. 8, can be used to calculate the values of m and k by regression analysis. The averages values of m and k are determined to be 2.11 and -0.957, respectively. Then, the DRX kinetics model of the HSLA steel is as follows:

$$X_d = 1 - \exp\left[(-0.975) \cdot \left(\frac{\varepsilon - \varepsilon_p}{\varepsilon_p}\right)^{2.11}\right]. \quad (18)$$
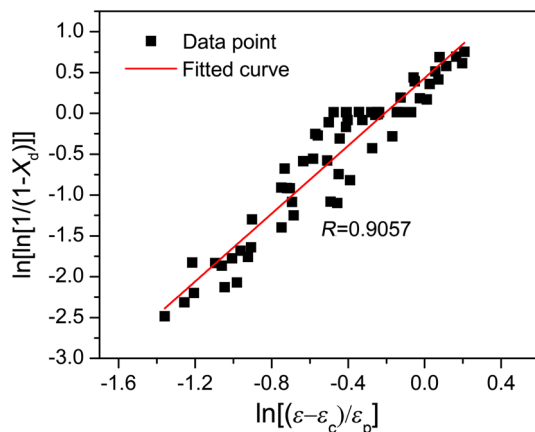

Fig. 8 Relationship between $\ln[\ln[1/(1-X_d)]]$ and $\ln[(\varepsilon-\varepsilon_c)/\varepsilon_p]$

The effects of deformation temperature, strain and strain rate on the recrystallized volume fraction are shown in Fig. 9a–c. All the curves exhibit S-shapes. The volume fraction of DRX increases with increasing temperature and stress, due to the increase in the driving force for DRX when the stress rate decreases and deformation temperature increases; the volume fraction of DRX enters the steady-state stage when a constant value of $X_d = 1$ is reached, which represents a completely new DRX process. Comparing these curves with one another, the DRX volume fraction increases with increasing temperature, which is consistent with the effect of temperature on the peak values of the flow curves. In contrast, for a fixed temperature, the deformation strain required for the same DRX volume fraction increases with increasing strain rate, which also means that DRX is delayed for a longer time. This effect can be attributed to the decreased mobility of grain boundaries (growth kinetics) with increasing strain rate and decreasing temperature. Thus, under higher strain rates and lower temperatures, the deformed metal tends toward incomplete DRX, that is to say, the DRX volume fraction tends to be less than 1. Furthermore, the experimental curves are also presented in the dot form to facilitate the comparison. A good agreement is recognizable, which in the present work also confirms that the kinetics model can predict DRX volume fractions of the HSLA with high accuracy.

Figure 10 shows the microstructures of HSLA steel at the strain rate of 0.1 s^{-1} and various temperatures. The grain sizes increase with increasing deformation temperature. At deformation temperatures of 800–900 °C, the grains are broken and elongated, as shown in Fig. 10a, b. DRX has partially occurred, and the grain distribution is heterogeneous. Most recrystallized sites are composed of necklace structure, which is strongly dependent on the
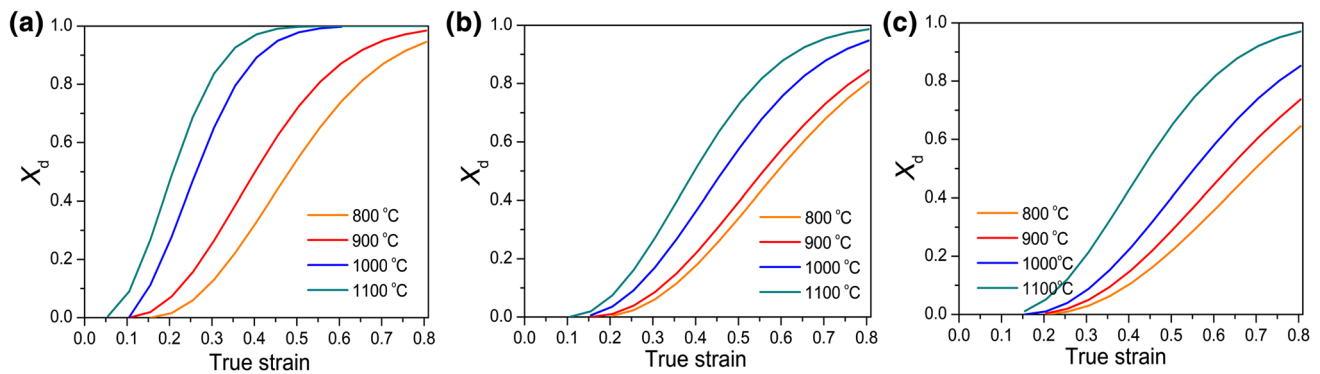
Fig. 9 Predicted volume fractions of DRX at strain rates of **a** 0.1 s^{-1}, **b** 1 s^{-1}, **c** 10 s^{-1}
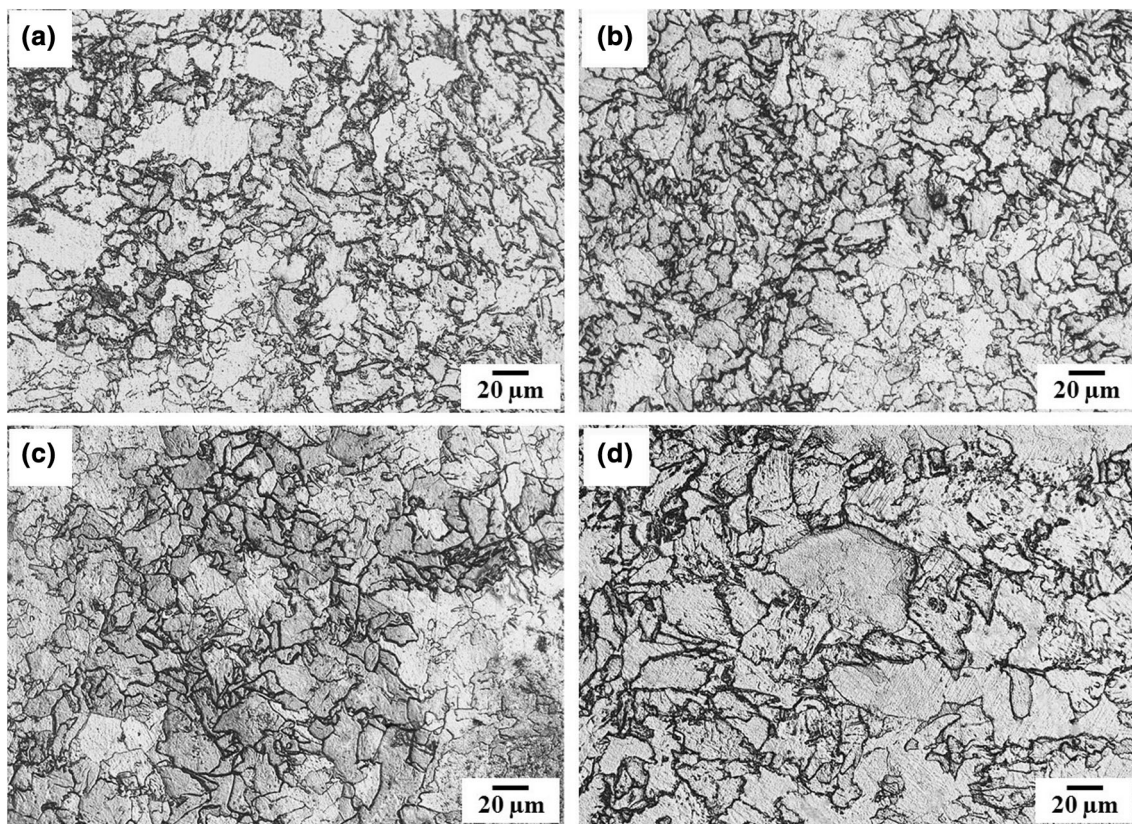

Fig. 10 Micrographs of HSLA steel deformed at **a** 800 °C, **b** 900 °C, **c** 1000 °C, **d** 1100 °C with strain rate of 0.1 s^{-1}

crystallographic orientation of the grain. Since the gradients near the grain boundaries provide potential nucleation sites for DRX, DRX generally initiates at grain boundaries and eventually replaces the original grains [41]. At a deformation temperature of 1100 °C, DRX is completely finished, and the DRX grains have a homogeneous distribution, as shown in Fig. 10d. Combining with the DRX volume fraction in Fig. 10, the condition at deformation temperature range of 1000–1100 °C and strain rate of 0.1 s^{-1} are appropriate for hot deformation of the experimental HSLA steel and can be confirmed by the DRX

volume fraction increases with increasing deformation temperature and decreasing strain rate [42] as shown in Fig. 10.
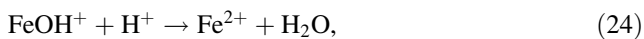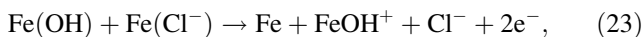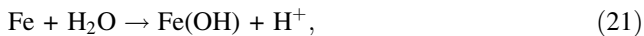
3.5 Corrosion Behavior

The electrochemical corrosion behavior of a metallic surface is extremely complex and depends on the metallurgical microstructure and surface morphology factors. Microstructure plays a role through the electrochemical behavior of constituent intermetallic particles, while the

morphology of the surface, particularly roughness, provides sites of enhanced reactivity as well as occluded sites for corrosion [43]. Figure 11a shows localized corrosion on HSLA steel at a deformation temperature 800 °C and a strain rate of 0.1 s^{-1} after a potentiodynamic polarization test in 1.0 mol/L. This form of corrosion is extremely localized corrosion or pitting-type corrosion and manifests as holes on the metal surface, and as included in Fig. 11b is the model for the pitting mechanism. Pitting corrosion may occur due to the breakdown of a protective film (passive oxide film). It is well known that the corrosion of HSLA steel is a dissolution process that involves a cathodic reaction and anodic reaction. The reaction equations are listed as follows [44]:

$$Fe \rightarrow Fe^{2+} + 2e^-, \tag{19}$$

$$2H_2O + O_2 + 4e^- \rightarrow 4OH^-. \tag{20}$$
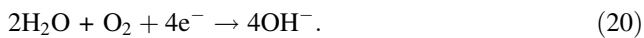
The dissolution of iron into ferrous cations in concentrated NaCl solution can be described as follows:

$$Fe + H_2O \rightarrow Fe(OH) + H^+, \tag{21}$$

$$Fe + Cl^- \rightarrow Fe(Cl^-), \tag{22}$$

$$Fe(OH) + Fe(Cl^-) \rightarrow Fe + FeOH^+ + Cl^- + 2e^-, \tag{23}$$

$$FeOH^+ + H^+ \rightarrow Fe^{2+} + H_2O, \tag{24}$$

The equations for the formation of the corrosion products are as follows:

$$Fe + 1/2O_2 + H_2O \rightarrow Fe(OH)_2, \tag{25}$$

$$Fe(OH)_3 \rightarrow FeOOH + H_2O. \tag{26}$$
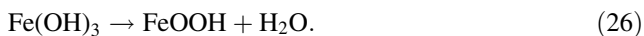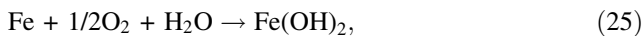
According to the behavior of iron in a high concentration of Cl^-, the presence of Cl^- is conducive to the formation of FeOOH (rust) [45]. The formation of iron oxides as the product of the chemical reactions presented by Eqs. (23)–(26) is possible for the HSLA steel specimen in 1 mol/L NaCl solution.

The effects of increasing the deformation temperature during hot compression processing of the HSLA steel in 1 mol/L NaCl solutions are investigated using potentiodynamic polarization measurements. The potentiodynamic polarization curves obtained for the HSLA steel after hot deformation at various compressive parameters in 1.0 mol/L NaCl solutions are shown in Fig. 12. No obvious active–passive transition potential peaks are observed in the NaCl solution, which indicates highly aggressive behavior from the solution. The anodic current varies significantly with increasing cooling rate. The fitted electrochemical corrosion kinetics parameters, including anodic Tafel constants (β_a), cathodic Tafel constants (β_c), corrosion potentials (E_{corr}), corrosion current densities (i_{corr}), and corrosion rates (R_{corr}), are presented in Table 2.

The potentiodynamic polarization curves shift toward higher corrosion current density values with increasing temperature. The specimens deformed at low temperature show lower values of i_{coor} than those of the specimens
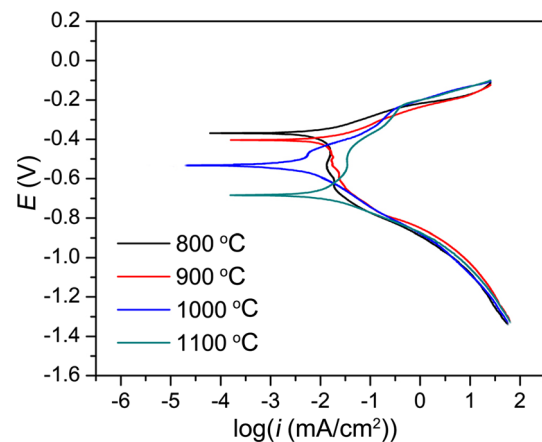

Fig. 12 Potentiodynamic polarization curves for HSLA steel at a strain rate of 1 s^{-1} in 1.0 mol/L NaCl solution (*E*: potential; *i*: current density)
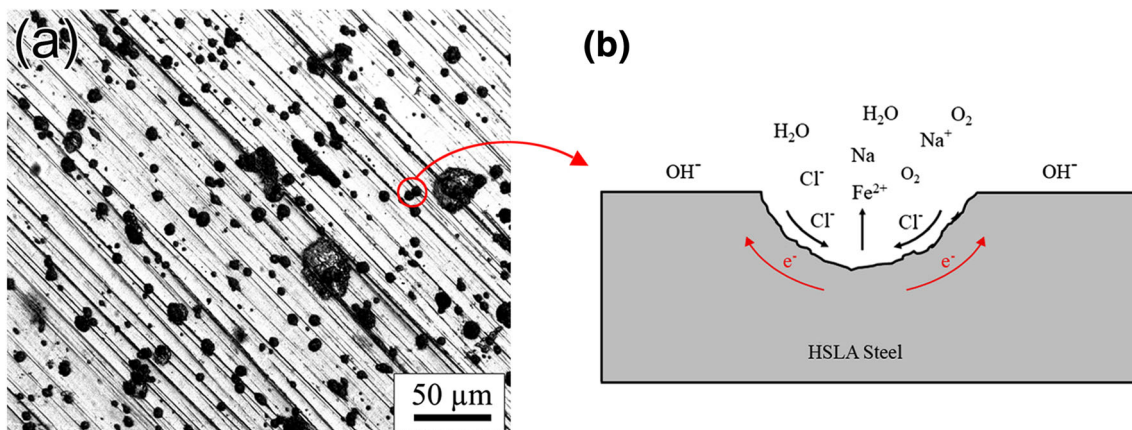

Fig. 11 **a** Localized corrosion on HSLA steel after potentiodynamic polarization in 1.0 mol/L NaCl, **b** schematic for pitting mechanism

Table 2 Potentiodynamic polarization parameters obtained from curve fitting of HSLA steel at strain rate of 0.1 s^{-1}

Condition (°C)	E_{corr} (mV)	i_{corr} (μA/cm^2)	β_a (V/dec)	β_c (V/dec)	R_{corr} (mpy)
800	−369.63	10.642	0.080	0.786	4.67
900	−395.31	11.419	0.081	0.616	5.02
1000	−532.84	14.194	0.457	0.146	6.24
1100	−692.11	16.705	0.501	0.101	7.34

deformed at high temperature. The specimens deformed in compression tests at 800 °C and a strain rate of 0.1 s^{-1} have the lowest i_{corr} value of 4.67 μA/cm^2, while the specimens deformed at higher temperatures of 1000–1100 °C have the highest i_{corr} values of 6.24 and 7.34 μA/cm^2. Deformation at low temperature may improve the corrosion resistance of specimens, which would be consistent with the results in Ref. [46], that inhibiting recrystallization possibly enhances stress corrosion resistance in Al–Zn–Mg–Cu–Zr alloys. As discussed in the section above, more crystallized grain structures with large grain boundaries are formed at 1000 and 1100 °C. In general, an increase in the quantity of grain boundaries leads to an increase in anodic reactions, which affects the occurrence of DRX during deformation [27, 47]. Thus, the large number of grain boundaries contributes to the low corrosion resistance, and the corrosion rate of specimens also increases with increasing corrosion current density.

4 Conclusion

Hot compression tests on HSLA steel were performed under various deformation conditions. The stress–strain data, dynamic recrystallization characteristics, and corrosion behavior were carefully analyzed. The main conclusions drawn are as follows:

1. The true stress–strain curves of HSLA steel under various conditions show characteristic dynamic recrystallization behavior in relation to the strain rate and temperature. The flow stress increases with decreasing deformation temperature and increasing strain rate.

2. The activation energy is calculated to be 351.87 kJ/mol, and the relationships between the characteristic points σ_c (ε_c), σ_p (ε_p) and σ_{ss} and the Z parameter are identified. The peak strain (ε_p) and stress (σ_p) can be expressed as power-law functions of Z and are determined to be $\sigma_p = 9.68\ Z^{0.07}$ and $\varepsilon_p = 0.033\ Z^{0.061}$ for the HSLA steel.

3. The final optimized deformation process conditions to obtain a completely recrystallized and homogeneously distributed microstructure include a deformation temperature in the range of 1000–1100 °C and a strain rate of 0.1 s^{-1}. The DRX kinetic model of HSLA steel is

obtained. The volume fractions of DRX grains calculated by the model are in good agreement with those of the experimental results, indicating that the model is suitable for predicting the DRX process of the steel.

4. The corrosion behavior of HSLA in 1.0 mol/L NaCl solutions was investigated using potentiodynamic polarization measurements. The specimens deformed at low temperatures (800–900 °C) are more corrosion resistant than the specimens deformed at high deformation temperatures (1000–1100 °C).

References

[1] S.L. Chawla, R.K. Gupta, *Materials Selection for Corrosion Control* (ASM International, Metals Park, OH, 1993)
[2] H.K.D.H. Bhadeshia, R. Honeycomb, *Steels Microstructure and Properties*, 3rd edn. (Elsevier, London, 2006)
[3] W. Yuan, B. Zhou, Y. Tang, Z.C. Zhang, J. Deng, Int. J. Miner. Metall. Mater. **21**, 913 (2014)
[4] J.M. Zhang, W.H. Sun, S. Hao, J. Iron. Steel Res. Int. **17**, 63 (2010)
[5] D.P. Li, L. Zhang, J.W. Yang, M.X. Lu, J.H. Ding, M.L. Liu, Int. J. Miner. Metall. Mater. **21**, 388 (2014)
[6] L. Niu, Y.F. Cheng, Appl. Surf. Sci. **253**, 8626 (2007)
[7] C.H. Liang, C.H. Cao, N.B. Huang, Int. J. Miner. Metall. Mater. **19**, 328 (2012)
[8] M. Alizadeh, S. Bordbar, Corros. Sci. **70**, 170 (2013)
[9] K. Aramaki, T. Shimura, Corros. Sci. **46**, 2563 (2004)
[10] J. Stiksma, S.A. Bradford, Corrosion **41**, 446 (1985)
[11] D.A. López, W.H. Schreiner, S.R. de Sánchez, S.N. Simison, Appl. Surf. Sci. **207**, 69 (2003)
[12] S. Bordbar, M. Alizadeh, S.H. Hashemi, Mater. Des. **45**, 597 (2013)
[13] Y.L. Zhang, M. Du, J. Zhang, J.Q. Du, Mater. Corros. **66**, 366 (2015)
[14] J. Huo, Y.C. Liu, D.T. Zhang, Z.S. Yan, Z.M. Gao, Steel Res. Int. **84**, 184 (2013)
[15] Y. Zhang, H. Sun, A.A. Volinsky, B. Tian, K. Song, B. Wang, Y. Liu, Vacuum **146**, 35 (2017)
[16] J.J. Jonas, Mater. Sci. Eng. A **184**, 155 (1994)
[17] G.R. Stewart, J.J. Jonas, F. Montheillet, ISIJ Int. **44**, 1581 (2004)
[18] N.D. Ryan, H.J. McQueen, Can. Metall. Q **29**, 147 (1990)
[19] S. Saadatkia, H. Mirzadeh, J.M. Cabrera, Mater. Sci. Eng. A **636**, 196 (2015)
[20] S.M. Abbasi, A. Shokuhfar, Mater. Lett. **61**, 2523 (2007)
[21] F.Z. Hassani, M. Ketabchi, G.R. Ebrahimi, S. Bruschi, Mater. Sci. Eng. A **657**, 383 (2016)

[22] T. Sakai, A. Belyakov, R. Kaibyshev, H. Miura, J.J. Jonas, Prog. Mater Sci. **60**, 130 (2014)

[23] A. Dehghan-Manshadi, P.D. Hodgson, ISIJ Int. **47**, 1799 (2007)

[24] Y. Zhang, H.L. Sun, A.A. Volinsky, B.H. Tian, Z. Chai, P. Liu, Y. Liu, Acta Metall. Sin. (Engl. Lett.) **29**, 422 (2016)

[25] W. Gao, A. Belyakov, H. Miura, T. Sakai, Mater. Sci. Eng. **265**, 233 (1999)

[26] F.T. Kong, N. Cui, Y.Y. Chen, X.P. Wang, N.N. Xiong, Intermetallics **55**, 66 (2014)

[27] E. Zhang, Y. Ge, G. Qin, J. Mater. Sci. Technol. **34**, 523 (2018)

[28] W.Y. Liu, H. Zhao, D. Li, Z.Q. Zhang, G.J. Huang, Q. Liu, Mater. Sci. Eng. A **596**, 176 (2014)

[29] J. Wang, H.T. Yang, X.G. Wang, H. Xiao, Mater. Des. **65**, 637 (2015)

[30] G. Biao, S.C. Zhang, C.C. Ge, J. Iron. Steel Res. Int. **21**, 389 (2014)

[31] H. Wu, L. Du, X. Liu, J. Mater. Sci. Technol. **27**, 1131 (2011)

[32] E.I. Poliak, J.J. Jonas, ISIJ Int. **43**, 684 (2003)

[33] G.R. Ebrahimi, H. Keshmiri, A.R. Maldar, A. Momeni, J. Mater. Sci. Technol. **28**, 467 (2012)

[34] M. Shaban, B. Eghbali, J. Mater. Sci. Technol. **27**, 359 (2011)

[35] G.R. Ebrahimi, H. Keshmiri, A. Momeni, M. Mazinani, Mater. Sci. Eng. A **528**, 7488 (2011)

[36] H.L. Wei, G.Q. Liu, H.T. Zhao, M.H. Zhang, Mater. Sci. Eng. A **596**, 112 (2014)

[37] Y. Xu, D. Tang, Y. Song, X. Pan, Mater. Des. **39**, 168 (2012)

[38] B. Zhao, T. Zhao, G. Li, Q. Lu, Mater. Sci. Eng. A **604**, 117 (2014)

[39] G.R. Stewart, A.M. Elwazri, S. Yue, J.J. Jonas, Mater. Sci. Technol. **22**, 519 (2006)

[40] J. Wang, H. Xiao, H.B. Xie, X.M. Xu, Y.N. Gao, Mater. Sci. Eng. A **539**, 294 (2012)

[41] R.O. Kaibyshev, B.K. Solokov, Phys. Met. Metall. **741**, 72 (1992)

[42] H.Q. Huang, H.S. Di, N. Yan, J.C. Zhang, Y.G. Deng, R.D.K. Misra, J.P. Li, Acta Metall. Sin. (Engl. Lett.) **31**, 503 (2018)

[43] P.O. Acevedo-Hurtado, P.A. Sundaram, J. Mater. Eng. Perform. **26**, 69 (2017)

[44] Y.B. Guo, C. Li, Y.C. Liu, L.M. Yu, Z.Q. Ma, C.X. Liu, H.J. Li, Int. J. Miner. Metall. Mater. **22**, 604 (2015)

[45] Y. Ma, Y. Li, F. Wang, Corros. Sci. **51**, 1725 (2009)

[46] M.B. Kannan, V.S. Raja, Eng. Fract. Mech. **77**, 249 (2010)

[47] G. Liu, W. Xie, G. Wei, Y. Yang, J. Liu, T. Xu, W. Xie, X. Peng, Materials **11**, 408 (2018)

[48] B.S. Xie, Q.W. Cai, W. Yu, L.X. Xu, Z. Ning, Acta Metall. Sin. (Engl. Lett.) **30**, 250 (2017)

[49] Q. Guo, H.G. Yan, H. Zhang, Z.H. Chen, Z.F. Wang, Mater. Sci. Technol. **21**, 11 (2005)